Three-Dimensional Modeling of the Deflagration Stage of a Type Ia Supernova Explosion

A. M. Khokhlov

Laboratory for Computational Physics and Fluid Dynamics,
Naval Research Laboratory, Washington, DC 20375

Abstract

The paper describes a physical model and numerical algorithm for modeling Type Ia supernova (SNIa) explosions in three-dimensions and presents first results of modeling a deflagration explosion in a non-rotating, Chandrasekhar-mass carbon-oxygen (CO) white dwarf. Simulations show that the turbulent flame speed grows exponentially, reaches $\simeq 30\%$ of the speed of sound, and then declines as the large-scale turbulence is frozen by expansion. The freezing of turbulent motions appears to be a crucial physical mechanism regulating the rate of deflagration in SNIa. The energy of the explosion is comparable to that of a typical SNIa. However, the presence of the outer layer of unburned CO and the formation of intermediate mass elements and pockets of unburned CO near the center pose problems for the modeling of SNIa spectra. Delayed detonation is a way to alleviate these problems and to produce consistent spectra.

1. Introduction

Type Ia Supernovae (SNIa) are thought to be thermonuclear explosions of Chandrasekhar-mass carbon-oxygen white dwarfs (CO-WD). They play an important role in nucleosynthesis (Nomoto et al. 1984) and the balance of energy in interstellar medium, and they are important distance indicators used in cosmology (Perlmuter et al., 1999; Riess et al. 2000). Our understanding of SNIa explosions is far from complete. To predict the explosion outcome, one needs to know how thermonuclear burning propagates inside the exploding star. The mechanisms and the speed of thermonuclear burning in SNIa remain an unsolved theoretical problem. A recent review by Hillebrandt & Niemeyer (2000) contains a large list of relevant publications.

Burning can propagate in a supernova either as a flame caused by the electron heat conduction or as a detonation in which reactions are triggered by a shock. Both the detonation speed and the laminar flame speed S_l in SNIa are known. However, in the gravitational field of the star, the laminar flame becomes unstable with respect to the Rayleigh-Taylor (RT) instability (Nomoto et al. 1976). This leads to a turbulent deflagration with some unknown turbulent flame speed $S_t > S_l$.

Observations indicate that burning of a Chandrasekhar-mass CO-WD must start as a deflagration. Spectra of SNIa at maximum light show the presence of large amounts of intermediate mass elements such as Si, S, Mg (Pskovskii 1977, Branch 1981). These elements can only be synthesized at densities less than $\simeq 10^7$g/cc, where the temperature of burned products stays below $\simeq (4-5)\times 10^9$K. When burning starts as a deflagration, the initially high-density WD expands while it burns, its density decreases, and this creates the necessary conditions for the production of intermediate mass elements. In one-dimensional deflagration models, S_t is a free parameter (Nomoto et al. 1976, Woosley & Weaver 1986). Delayed detonation models assume that a deflagration undergoes a transitions to a detonation at low densities (Khokhlov 1991). In these models, both S_t and the moment of a deflagration-to-detonation transition (DDT) are free parameters. To fit observations, burning must be initially slow in order to expand the WD significantly. Then burning must accelerate quickly to incinerate expanding outer layers rapidly. This requires very carefully tuning S_t as a function of time in deflagration models. Delayed-detonation models accomplish the incineration by switching to a supersonic detonation mode of burning.

Two-dimensional simulations of SNIa explosions show that burning leads to a significant expansion of a WD. However, the deflagration speed found in all of the simulations is too small to lead to a powerful explosion (Livne, 1993; Arnett & Livne, 1994; Reinecke et al., 2000). Whether this is an inherent difficulty of the deflagration model or simply a deficiency of two-dimensional simulations is a question. Two-dimensional simulations lack a key physical ingredient of turbulent burning – turbulent energy cascade that is directed in three dimensions from large to small spatial scales. Simulations of burning in a vertical column in a uniform gravitational field show that the turbulent flame speed grows faster in three dimensions and eventually reaches a turbulent steady state where S_t becomes independent of S_l and of the details of burning on small scales (Khokhlov, 1995; hereafter K95). In two dimensions, S_t grows more slowly and depends on the value of S_l. However, turbulence in the exploding star is affected by expansion on spatial scales $\mathcal{L}$, where the characteristic RT timescale $\tau_{RT} \simeq (g\mathcal{L})^{1/2}$ is comparable or exceeds the expansion timescale $\tau_e \simeq R/U_e$, where R is stellar radius and U_e is the (time-dependent) expansion velocity. Expansion tends to freeze large-scale turbulent motions and thus decreases the turbulent flame speed (K95). The actual S_t in a supernova must depend on the competition of the RT instability, turbulent energy cascade, and expansion. To predict S_t, these effects must be modeled in three dimensions. This paper describes a physical model and numerical algorithm for modeling SNIa explosions in three-dimensions and presents first results of modeling a deflagration explosion in a nonrotating, Chandrasekhar-mass CO-WD.

2. Physical and numerical model

2.1. Fluid dynamics

Stellar matter is described by the Euler equation for an inviscid fluid

$$\begin{aligned} \frac{\partial \rho}{\partial t} &= -\nabla \cdot (\rho \mathbf{U}) \ , \\ \frac{\partial \rho \mathbf{U}}{\partial t} &= -\nabla \cdot (\rho \mathbf{U}\mathbf{U}) - \nabla P + \rho \mathbf{g} \ , \\ \frac{\partial E}{\partial t} &= -\nabla \cdot (\mathbf{U}\,(E+P)) + \rho \mathbf{U} \cdot \mathbf{g} + \rho \dot{q} \ , \end{aligned} \tag{1}$$

where ρ, $E = E_i + \rho U^2/2$, E_i, $\mathbf{U}$, $\mathbf{g}$ and $\dot{q}$ are the mass density, energy density, internal energy density, velocity of matter, gravitational acceleration, and nuclear energy release rate per unit mass, respectively. The acceleration of gravity is computed using an angle-averaged density distribution. The equation of state (EOS) of degenerate matter includes contributions from ideal Fermi-Dirac electrons and positrons, equilibrium Planck radiation, and ideal ions. Pressure $P = P(\rho, E_i, Y_e, Y_i)$ and temperature $T = T(\rho, E_i, Y_e, Y_i)$ are determined by the EOS as functions of ρ, E_i, electron mole fraction Y_e, and the mean mole fraction of ions Y_i.

2.2. Flame propagation

The flame is advanced using a flame-capturing technique which mimics a flame with a prescribed normal speed (K95). A scalar variable f, such that $f = 0$ in the unburned matter and $f = 1$ in the material which has passed through the flame, obeys a reaction-diffusion equation

$$\frac{\partial f}{\partial t} + \mathbf{U} \cdot \nabla f = K \nabla^2 f + R \ , \tag{2}$$

with artificial reaction and diffusion coefficients

$$\begin{aligned} R &= \begin{cases} C = \text{const.}, & \text{if } f_0 \le f \le 1; \\ 0, & \text{otherwise,} \end{cases} \\ K &= \text{const}, \end{aligned} \tag{3}$$

with some $0 < f_0 < 1$. In this paper, $f_0 = 0.3$. Equation (2) has a solution $f(x - St)$ which describes a reaction front that propagates with the speed $S = (KC/f_0)^{1/2}$ and has a thickness $\delta \simeq (K/C)^{1/2}$ (see Appendix of (K95)). If K and C in (3) are set to

$$K = S(\beta \Delta r)\sqrt{f_0} \ , \qquad C = \frac{S}{(\beta \Delta r)}\sqrt{f_0} \ , \tag{4}$$

with β = constant, the front propagates with a prescribed speed S and spreads onto several computational cells of size Δr. The choice of $\beta = 1.5$ spreads the flame on $\simeq 3-4$ cells. Making the front narrower is not practical, since the fluid dynamics algorithm spreads contact discontinuities on $\simeq 4$ cells. The energy-release rate inside the front is defined as

$$\dot{q} = q_f \frac{df}{dt} \ , \tag{5}$$

where q_f, defined below in Section 3.4, is the nuclear energy release inside the front. Due to the energy release, both density and velocity vary across the front, and fluid motions are generated which advect the flame relative to the computational mesh. The flame-capturing technique described above advances the reaction front relative to the fuel with the speed practically independent of the orientation of the front on the mesh, fluid motions, and resolution.

2.3. Burning on small scales

A turbulent flame in a vertical column of width $\mathcal{L}$ subjected to an acceleration of gravity g propagates in a steady-state with the speed $S_t \simeq 0.5\sqrt{Ag\mathcal{L}}$ independent of the laminar speed S_l, where $A = (\rho_0 - \rho_1)/(\rho_0 + \rho_1)$ is the Atwood number, and ρ_0, ρ_1 are the densities ahead and behind the flame front, respectively (K95). The time to reach a steady state is $\simeq 2\mathcal{L}/S_t$, and the thickness of the flame brush is $\simeq 2\mathcal{L}$. To describe burning on scales that are not resolved in the simulations, the value of S in (4) is taken as

$$S = \max(S_l, S_{sub}) \ , \tag{6}$$

with

$$S_{sub} = 0.5\sqrt{A\,\alpha\Delta r\ (s_1|\mathbf{g}| + s_2 \max(0, \mathbf{n}\cdot\mathbf{g}))} \tag{7}$$

based on the assumption that burning on small scales is driven by the RT instability at these scales and that at $\mathcal{L} << R_{WD}$ burning adjusts to a local steady state (Livne 1993, Arnett & Livne 1994, K95). In (7), $\alpha \simeq 1$ determines the driving scale, $\mathcal{L} \simeq \alpha\Delta r$, in terms of the computational cell size Δr, and $\mathbf{n} = \nabla f/f$ is the unit vector normal to the flame front and directed towards the products of burning. The choice of $s_1 = 1$, $s_2 = 0$ gives a subgrid flame speed that is independent of the orientation of the flame front relative to the direction of gravity. The choice $s_1 = 0$, $s_2 = 1$ gives a directional-dependent speed that reduces to S_l when the flame moves in the direction of gravity. Finally, $s_1 = s_2 = 0$ gives the laminar flame speed. In this paper, only the limiting, angle-independent and laminar prescriptions for S were used. The Atwood number $A \simeq (\gamma - 1)\,\bar{\rho}\,q_f\,/\,2\gamma P$ was calculated from conservation of enthalpy, assuming constant pressure across the flame, where γ and $\bar{\rho} = (\rho_1 + \rho_0)/2$ are average values of the adiabatic index and mass density. Under the conditions of interest here, $A \simeq 0.1 - 0.4$. The laminar flame speed S_l, taken according to Timmes & Woosley (1992) and Khokhlov et al. (1997), is $S_l \simeq (10^{-2} - 10^{-4}) \times a_s$ for $\rho \simeq 10^9 - 10^7$g/cc, where $a_s \simeq 5 \times 10^8$cm/s is the sound speed.

2.4. Nuclear kinetics

There are three distinct stages of carbon burning. First, the $^{12}C + {}^{12}C$ reaction leads to the consumption of ^{12}C and formation of mostly ^{20}Ne, ^{24}Mg, protons and α-particles. Then the onset of the nuclear statistical quasi-equilibrium (NSQE) takes place, during which Si-group (intermediate mass) elements are formed. Finally, Si-group elements are converted into the Fe-group elements and the nuclear statistical equilibrium (NSE) sets in. The NSQE and NSE relaxation involves hundreds of species from carbon to zinc and thousands of reactions of these nuclei with protons, neutrons, and α-particles. The timescales of all these stages strongly depend on temperature. The timescale of carbon consumption is much shorter than the quasi-equilibrium timescale τ_{nsqe} which, in turn, is much shorter than the NSE timescale τ_{nse}.

A four-equation kinetic scheme is used here to describe the energy release, synthesis of Si- and Fe-group elements, and the neutronization of NSE matter. A similar scheme has been used in

one-dimensional simulations of SNIa (Khokhlov 1991). The kinetic equation for the mole fraction of carbon Y_C

$$\frac{dY_C}{dt} = -\rho A(T_9) \exp(-Q/T_{9a}^{1/3}) Y_C^2 \ , \tag{8}$$

describes carbon consumption through the major reactions $^{12}C\,(\,^{12}C,\,p)\,^{23}Na\,(\,p,\gamma)\,^{24}Mg$ and $^{12}C\,(\,^{12}C,\,^{4}He)\,^{20}Ne$ with the branching ratio $\simeq 1$. Here $Q = 84.165$, $T_{9a} = T_9/(1 + 0.067T_9)$, where $A(T_9)$ is a known function (Fowler et al. 1975).

Most of the nuclear energy is released during the carbon exhaustion stage and the subsequent synthesis of the Si-group nuclei. The energy release or consumption due to the transition from Si-group to Fe-group nuclei (NSE relaxation) is less than 10%. Therefore, the nuclear energy release rate is approximated as

$$\frac{dq_n}{dt} = -Q_C \frac{dY_C}{dt} + \frac{q_{nse} - q_n}{\tau_{nsqe}} \ , \tag{9}$$

where $q_n(t)$ is the binding energy of nuclei per unit mass, $Q_C = 4.48 \times 10^{18}$ ergs g^{-1} mol^{-1} is the energy release due to carbon burning (8), and $q_{nse}(\rho, T, Y_e)$ is the binding energy of matter in the state of NSE.

The equation

$$\frac{d\delta_{nse}}{dt} = \frac{1 - \delta_{nse}}{\tau_{nse}} \ , \tag{10}$$

traces the onset of NSE, where $\delta_{nse} = 0$ in the unburned matter and $\delta_{nse} = 1$ in the NSE products. Intermediate mass elements are expected where $Y_C(t = \infty) \simeq 0$ and $\delta_{nse}(t = \infty) < 1$. Fe-group elements are expected where $Y_C(t = \infty) \simeq 0$ and $\delta_{nse}(t = \infty) \simeq 1$. The 'e-folding' NSQE and NSE timescales

$$\begin{aligned} \tau_{nsqe} &= \exp\left(149.7/T_9 - 39.15\right) \ \mathrm{s} \ , \\ \tau_{nse} &= \exp\left(179.7/T_9 - 40.5\right) \ \mathrm{s} \ , \end{aligned} \tag{11}$$

approximate the results of the detailed calculations of carbon burning. The original kinetic scheme (Khokhlov 1991) also contained the equation for the mean ion mole fraction Y_i. To simplify the scheme in this paper, variations of Y_i due to nuclear reactions were neglected since ions make a small contribution to the equation of state. A constant $Y_i = 0.07$ was used instead, which is an average of Y_i in the unburned and typical NSE matter in the SNIa explosion conditions.

Neutronization is described by the equation for the electron mole fraction Y_e,

$$\frac{dY_e}{dt} = -R_w(\rho, T, Y_e) \ . \tag{12}$$

The corresponding term describing neutrino energy losses, $-\dot{q}_w(\rho, T, Y_e)$, is added to the energy conservation equation in (1). Values of q_{nse}, $\dot{q}_w$, and R_w were computed assuming NSE distribution of individual nuclei, as described in (Khokhlov 1991). Recently, there has been an important development in theoretical computations which shows significantly smaller electron capture and β-decay rates in stellar matter (Langanke et al. 1999 and references therein). Following Martinez-Pinedo et al. (2000), this effect was approximately taken into account by decreasing $\dot{q}_w$ and R_w by a factor of 5. This should be sufficient to account for changes in q_{nse} and in the corresponding nuclear energy release $q_{nse} - q_n(t = 0)$ caused by variations of Y_e. In future simulations, we plan to use $\dot{q}_w$ and R_w based on the new individual capture rates.

Despite its simplicity, the kinetic scheme reasonably well describes all major stages of carbon burning. In particular, it takes into account the important effect of energy release or absorption caused by changes in NSE composition when matter expands or contracts (these changes happen on a quasi-equilibrium rather than on the equilibrium timescale). When the WD expands, this

effect adds $\simeq 50\%$ to the energy initially released by burning at high densities. Using even the simplest 13-species α-network to account for this effect would be prohibitively expensive in three-dimensional hydrodynamical simulations.

To couple the kinetic scheme and the front tracking algorithm (Section 2.2), q_f in (5) is taken $q_f = q_{nse} - q_n(0)$ at densities $\rho > 2 \times 10^7$ g/cc, $q_f = Q_C Y_C(t = 0)$ at $\rho < 5 \times 10^6$ g/cc, and is linearly interpolated between the two values in the density range $5 \times 10^6 - 2 \times 10^7$ g/cc. The carbon mole fraction Y_C inside the front is decreased in proportion to the increase of f. Thus, at high densities, both carbon consumption and the NSQE relaxation take place inside the flame front. At low densities where the NSQE stage of burning is slow, NSQE relaxation takes place outside the flame front.

2.5. Numerical method

Fluid dynamics equations (1) for ρ, $\mathbf{U}$, E, and advection parts of equations (2), (8)-(10) and 912) for chemical variables f, Y_C, q_n, δ_{nse} and Y_e are solved using an explicit, second-order, Godunov-type, adaptive mesh refinement algorithm ALLA (Khokhlov, 1998). A Riemann solver for an arbitrary EOS (Colella & Glaz, 1985) is used to evaluate fluxes at cell interfaces. Left and right states are computed using a monotone piecewise-linear reconstruction (van Leer 1979). A small amount of an artificial diffusion flux (Lapidus, 1967) is added to Euler fluxes following Colella and Woodward (1984). This feature is used only in the vicinity of strong shocks. Multidimensions are treated using directional splitting. The diffusion term in (2) is treated using an explicit, second-order finite differencing.

ALLA uses a fully threaded tree (FTT) adaptive mesh refinement to refine the computational mesh on the level of individual cells (Khokhlov 1998; Khokhlov & Chtchelkanova, 1999). FTT is a tree with inverted thread pointers directed from children to neighbors of parent cells. As opposed to conventional tree structures, all operations on the FTT, including tree modifications (refinement and unrefinement) are $O(N)$, where N is a number of cells. All of these operations can be performed in parallel. FTT has a $2\frac{1}{2}$ integers-per-cell memory overhead, compared with 8 integers for an ordinary tree or 14 integers for a tree that stores connectivity information. Computations using the FTT are virtually as fast (per computational cell) as those on a regular grid. A massively parallel version of the code uses a space-filling curve approach to maintain data locality, achieve load balance, and minimize interprocessor communications. ALLA has been extensively tested and used in various combustion problems involving shocks, flames, turbulence, and their interactions (Gamezo et al., 1999,2000; Khokhlov & Oran, 1999; and references therein) and in astrophysics (Khokhlov et al., 1999).

Mesh refinement was used to refine shocks, contact discontinuities, and regions with large gradients of ρ, P, and f. The expressions for the corresponding shock, ξ_s, discontinuity, ξ_c, and gradient refinement indicators, ξ_P, ξ_ρ, ξ_f, are given by the equations (11), (12) and (13) of Khokhlov (1998), respectively. In addition, refinement was introduced for the gradients of tangential velocity using an indicator

$$\xi_u = \max_{j,k=1,\ldots,3} \left((1 - \delta_{jk}) \left(\frac{\partial U_k}{\partial x_j} \right) \right) \frac{\Delta x}{\alpha \, a_s} \tag{13}$$

with $\alpha = 0.05$. Refinement was initiated in places where the maximum of all indicators,

$$\xi = \max(\xi_s, \xi_c, \xi_P, \xi_\rho, \xi_f, \xi_u) \ , \tag{14}$$

was larger than the threshold value $\xi > 0.5$. The mesh was unrefined in places where ξ was less than the threshold value $\xi < 0.05$. The cell size Δr is related to the level l of the cell in the tree as $\Delta r = L/2^l$. The mesh can be characterized by the minimum and maximum levels of leaves

(unsplit cells) in the tree, l_{min} and l_{max}, which were predefined at the beginning of a computation. During a computation, mesh refinement was allowed for cells with $l_{min} \leq l < l_{max}$.

Computations were carried out on a 128 250MHz R10000 SGI Origin 2000 at the Naval Research Laboratory (NRL). On this machine, ALLA advanced $\simeq 2 \times 10^4$ cells at the rate of one timestep per second per processor on pure fluid-dynamic, three-dimensional problems with γ held constant. With the addition of a degenerate matter EOS, flame capturing, and nuclear kinetics, the speed decreased to $\simeq 6 \times 10^3$ cell-steps/s/processor.

2.6. Problem setup and initial conditions

Most of the computation were performed for one octant of the WD assuming mirror symmetry along the $x = 0$, $y = 0$ and $z = 0$ planes passing through the WD center. The initial temperature was taken as $T = 10^5$K everywhere inside the WD. The initial central density was taken as $\rho_c = 2 \times 10^9$ g/cc. Starting from the central pressure $P(\rho_c)$, the equations of hydrostatic equilibrium, $dP/dr = -GM\rho/r^2$ and $dM/dr = 4\pi\rho r^2$, were integrated outward until $P = 0$ was reached. The resulting WD configuration was interpolated onto a three-dimensional mesh. Nuclear kinetic variables for the unburned matter and $f = 0$ were defined everywhere. To initiate burning in the center, $f = 1$ was then set inside a small sphere of radius $r_i = 3 \times 10^6$ cm and mass $M_i \simeq 8 \times 10^{-5} M_{WD}$. For a while, burning was not allowed inside the sphere in order not to impulsively disturb the hydrostatic equilibrium. This procedure smoothly triggered the flame propagation process just outside the sphere. Due to the finite numerical resolution, the shape of the initial flame bubble was not perfectly spherical but contained a number of perturbations. A quadrupole mode was the largest mode of perturbations consistent with the symmetries of the problem. Smaller perturbations were mostly burned out by the flame, but the quadrupole mode partially survived and gave rise to the development of the RT instability.

3. Results

3.1. Hydrostatic equilibrium

Before calculating flame propagation, tests were made to ensure that without burning, the WD remains hydrostatic and keeps its symmetry. Since a Chandrasekhar-mass WD is close to a collapse threshold, its equilibrium is very sensitive to the discretization errors. Thus a rather fine mesh is required near the WD center to maintain equilibrium. The initial mesh was constructed with fine cells at level $l = l_{max} = 10$ for radii $r < 0.4R_{WD}$, at $l = l_{max} - 1$ for $0.4R_{WD} \leq r < 0.8R_{WD}$, at $l = l_{max} - 2$ for $0.8R_{WD} \leq r < 1.1R_{WD}$, and coarser cells at larger r. Computations of hydrostatic equilibrium with $\Delta r(l_{max}) = 5 \times 10^5$ cm showed numerical noise $< 3 \times 10^5$cm/s everywhere except in the very outer layers of the WD where the density changed from cell to cell by more than an order of magnitude. Near the center, the noise was less than the fluid velocity generated by the laminar flame, $\simeq S_l(\rho_0 - \rho_1)/\rho_0 \simeq 2 \times 10^6$ cm/s. The total kinetic energy E_k of the WD remained $E_k < 10^{-5} E_{th}$, where E_{th} is the total internal energy, during more than two sound crossing times of the WD ($\simeq 0.9$ s of integration). Deviations from spherical symmetry were negligible.

3.2. Deflagration of a $0.5C + 0.5O$ WD

Deflagration of a CO-WD with initial composition $X_C = 0.5$ by mass ($Y_C = 1/24$), central density $\rho_c = 2 \times 10^9$g/cc, and angle-independent small scale burning $s_1 = 1$, $s_2 = 0$ and $\alpha = 1$ in (7), serves as the baseline case. The computational domain for this simulation had size $L = 5.35 \times 10^8$ cm with levels of refinement $l_{max} = 10$, $l_{min} = 7$, and with maximum and minimum resolution

$\Delta r(l_{max}) = 5.22 \times 10^5$ and $\Delta r(l_{min}) = 6.18 \times 10^6$ cm, respectively. The simulation was carried out for $\simeq 1.8$s of physical time using Courant number 0.7, required $\simeq 9,000$ timesteps, and took $\simeq 6,000$ CPU hours. The initial fixed mesh described in Section 3.1 was used for approximately 1s. After that, the mesh refinement was turned on. The number of cells used in the simulation grew from $\simeq 5,000,000$ in the beginning to $\simeq 30,000,000$ at the end of the simulation.

Figure 1 presents the evolution with time of the released nuclear energy E_n, kinetic energy E_k, binding energy E_{tot}, and burned mass M_b inside the WD. The figure shows that the deflagration resulted in a SNIa explosion. At 1.8s, about 1.3×10^{51} ergs has already been released and $E_{tot} \simeq 8 \times 10^{50}$ergs is positive (the WD is unbound). At this moment, the WD radius is $R_{WD} \simeq 4.7 \times 10^8$ cm, $\rho_c \simeq 7 \times 10^7$g/cc and the expansion velocity $U_{exp} \simeq 1.0 \times 10^9$ cm/s. Burning will probably release a few more units of 10^{50}ergs until central density reaches $\simeq 10^6$g/cc and burning quenches completely.

Figure 2 shows the time evolution of the flame surface. Initial perturbations lead to the formation of rising plumes of burned material. In the beginning, the flame surface and the energy release are small, and the flame growth takes place in essentially hydrostatic conditions. At $t < 1$s, the kinetic energy remains less that $\simeq 10^{47}$ ergs or $\simeq 0.01\%$ of the binding energy of the WD (Figure 1b). The flame surface increases significantly and becomes more wrinkled at later times. The energy release rate increases, and the WD begins to expand.

Figures 3 and 4 show the flame variable f and the distribution of radial velocity V_r at 1.44s in three orthogonal planes, $x = 3.2 \times 10^7$cm, $y = 3.2 \times 10^7$cm, and $z = 3.2 \times 10^7$cm, offset from the WD center. At this time the flame has approximately reached the half-radius of the WD. The figures illustrate several important features of burning. Outer parts of the flame consist of big plumes rising through the WD. The absolute velocity of these plumes is $\simeq 6 \times 10^8$cm/s or $\simeq a_s$. This is about two times larger than the overall expansion velocity of matter, $U_{exp} \simeq 3 \times 10^8$cm/s. The plume velocity relative to the expanding material, $\simeq 0.5 a_s$, is subsonic. Figure 4 also shows regions of unburned matter sinking to the center. There is a complex flow pattern close to the WD center where fresh fuel is burned by the flame and different parts of the flame collide with each other and annihilate. This is similar to turbulent burning in a vertical column in a uniform gravitational field (K95). In that case, the leading part of the flame is also dominated by large scale bubbles whose motions determine the amount of fuel passing through the flame. The fuel was burned inside the flame brush which is dominated by smaller-scale structures. Since the scale of the largest plumes in a column is limited by the column width, the flame is able to reach a steady state on all scales. In a spherical star, however, more space becomes available for the plumes as the flame moves to larger radii, and the rate of burning must increase with time.

Figure 5 shows the effective turbulent flame speed S_t which was estimated as the speed of an equivalent spherical flame burning matter with the same rate,

$$S_t \simeq \frac{1}{4\pi\rho r_f} \frac{dM_b}{dt} \ , \tag{15}$$

where r_f and ρ_f are the average radius and the density ahead of the flame brush. In the simulation, a small-scale flame speed S determined by (7) was $\simeq (1-2) \times 10^7$cm/s, depending on the radius, local density, and time. Figures 1 and 5 show that burning rate increased at $t < 1.4 - 1.5$s and noticeably exceeded the value of S due to the growth of the flame surface. However, S_t reached maximum at $\simeq 1.5$s and started to decline at later times. The WD becomes unbound soon after maximum S_t is reached (see Fig. 1).

Figures 6 and 7 show the flame and radial velocity at the end of the simulation, 1.8s. The leading part of the flame is still dominated by large plumes, whereas inner parts are wrinkled and contain more complex structures. The outer edge of the flame is located at $\simeq 0.8 R_{WD}$.

The absolute velocity of the plumes has increased and reached $\simeq 10^9$cm/s. However, the average expansion velocity of the WD has increased significantly and is also $U_{exp} \simeq 10^9$cm/s. The velocity of the flame bubbles is essentially zero relative to the expanding matter, and they have practically stopped rising. The expansion completely froze the RT-instability on large scales. Generation of new flame surfaces on large scales ceased. Freezing through expansion is the reason for decrease in burning rate at $t > 1.5$s.

There was an earlier three-dimensional computation of a deflagration explosion in a CO-WD (K95) that used a nonuniform expanding 185^3 grid, assumed instantaneous transition of burned matter to the state of NSE, and the same prescription for S as in this paper. This computation was terminated at $\simeq 1.7$s. At $\simeq 1.7$s, the simulation showed plumes of burned material rising at $\simeq 5 \times 10^8$cm/s. Approximately 35% of the matter was burned, in agreement with this paper (Note that M_b shown in Figure 16 of K95 must be multiplied by 8, as it erroneously shows the amount of burned matter as per one octant of the star). In the earlier calculation, the WD is still slightly bound.

To illustrate mesh refinement, Figure 8 shows the mesh in the X-Y plane $z = 3.2 \times 10^7$cm at 1.8s. Figure 9 shows the mesh, density and velocity field in a small region in the X-Z plane $y = 3.2 \times 10^7$cm with coordinates $x = 0 - 1.2 \times 10^8$cm, $z = 0 - 9.4 \times 10^7$cm. Despite the complexity of the flame surface and velocity field inside the flame brush, the overall expansion of the WD is remarkably one-dimensional. This is due to the subsonic nature of burning which allows pressure to equilibrate inside the WD. Small deviations of the WD surface from spherical symmetry are only noticeable at late times when the flame gets very close to it.

3.3. Importance of small-scale burning

Figure 10 shows the time evolution of E_n, E_k, E_{tot}, and M_b for the simulation of a $0.5C + 0.5O$ WD with $S_{sub} = 0$ in (6). All other parameters were the same as in the baseline case presented in Section 3.2. Flame development was similar in the beginning. However, in this case, burning slowed down and then practically stopped because the expansion decreased S_l by $\simeq 3$ orders of magnitude. There was no explosion in this case and the WD remained bound. This shows that some amount of burning on unresolved scales must be incorporated. Although $S \simeq 10^7$cm/s in the baseline case was too small to produce an explosion by itself, it is necessary to allow nuclear energy release at a flame front whose area increases due to turbulence. A finite S is also necessary to mimic the reduction in flame surface caused by merging and burnout of small-scale structures. This is crucial in order to reproduce numerically a self-similar regime of turbulent burning in which the burning rate becomes independent of the details of flame behavior on small scales (K95). Figure 11 compares the flame surface at $\simeq 1.3$s for both cases in the $X - Y$ plane passing through the center of the WD. This figure illustrates the tendency of the flame to create more surface when S is small and to create less surface when S increases. Simulations with more resolution and different prescriptions for S are required to determine if we are indeed beginning to see the self-similar behavior of the flame.

3.4. Nucleosynthesis

Figure 12 shows the distribution inside the WD of Fe-group, Si-group (intermediate mass elements), and unburned CO matter at 1.8s. The location of Si-group elements is determined using the criterion $\delta_{nse} < 0.95$ (equation (10)). The figure shows that unburned CO penetrates deep inside the flame brush and is present in significant amounts near the WD center. Incomplete burning and the formation of intermediate mass elements occur at densities less than $\simeq 10^7$g/cc and take place at radii greater than $\simeq 0.3 R_{WD}$. Closer to the center, the density is still too high,

and burning produces of Fe-group nuclei. The production of S-group nuclei will move inwards as the WD expands further. Pockets of completely unburned CO are likely to survive in central parts. Before burning quenches, one should also expect the formation of large amounts of magnesium in the central parts of the WD. In one-dimensional models magnesium only forms immediately before quenching of incomplete burning in the outer parts of the WD. here, outermost parts of the WD are expected to stay completely unburned since the penetration of the flame into the these layers has stopped (Section 3.2).

Figure 13 shows the distribution at 1.8s of the neutron excess of matter $\eta = 1 = 2Y_e$. The maximum neutron excess, $\eta \simeq 0.013$, is much smaller than $\simeq 0.1$ typically obtained in one-dimensional SNIa simulations (Nomoto et al, 1984; Woosley & Weaver, 1986; Khokhlov, 1991). This is mostly due to a reduction of the theoretical electron capture rates (Section 2.4). In addition, burned matter spends less time near the center due to RT-mixing. Figure 13 shows that the high-η products are present at radii up to $\simeq 0.8R_{WD}$.

3.5. Sensitivity to initial conditions

Figure 14 shows the results of a numerical experiment in which the location of the initial flame bubble was offset from the WD center by $\frac{1}{3}$ of its radius ($\simeq 10^6$cm). The computational domain was doubled, and a simplified flame propagation scheme with constant $q_f = q_{nse} - q_n(0)$ equal to the instantaneous NSE energy release was used. Equations (8)-(11) were turned off to save time. A 30% deviation of the ignition cite from the center was enough to cause a highly asymmetric flame.

In another numerical experiment the initial carbon mass fraction X_C was decreased from $X_C = 0.5$ (Case B) to $X_C = 0.2$. This resulted in less energy release and less buoyancy of burned products. Comparison between the $X_C = 0.5$ and $X_C = 0.2$ runs (Figure 15) shows a significant delay and slower increase of burning.

4. Discussion and conclusions

This paper described a physical model and an adaptive mesh refinement numerical algorithm for three-dimensional modeling of Type Ia supernovae. It also presented the first results of three-dimensional simulations using this model of a deflagration in a nonrotating, Chandrasekhar-mass, carbon-oxygen white dwarfs.

The simulation of a $0.5C + 0.5O$ CO-WD with central density $\rho = 2 \times 10^9$g/cc was carried out for $\simeq 1.8$s. The leading edge of the flame was dominated by large-scale, rising plumes of burned matter. Between these plumes, unburned CO was sinking towards the WD center. Fine-structured flame surface developed closer to the center below the plumes. The simulation lasted long enough to demonstrate the effect of freezing of large-scale turbulence due to expansion predicted in (K95). The effective turbulent burning speed S_t increased exponentially due to the growth of the RT-instability, reached maximum value $S_t \simeq 2 \times 10^8$ cm/s at $\simeq 1.5$s, and then started to decline. The expansion velocity of the WD reached $\simeq 10,000$km/s by the end of the simulation, and the motion of the buoyant plumes relative to unburned matter practically stopped.

The deflagration resulted in a rather healthy explosion. About 60% of the WD was burned by the end of the simulation, and this released $\simeq 1.3 \times 10^{51}$ergs of nuclear energy. The total energy, $E_{tot} \simeq 8 \times 10^{50}$ergs, was positive and the WD was unbound. By 1.8s, the WD radius was $\simeq 4.7 \times 10^8$cm, and burning still continued in its central parts. It should be expected that a few more units of 10^{50}ergs would be released before burning would be quenched completely, so that the total kinetic energy at infinity should be in the range $(1 - 1.3) \times 10^{51}$ergs. This is $\simeq 50 - 80\%$ of the kinetic energy required to produce a typical SNIa explosion. The total burned mass in this simulation is expected to be around $\simeq 1M\odot$. Detailed nucleosynthesis postprocessing is required

to predict the amount of ^{56}Ni synthesized during the explosion. By analogy with one-dimensional simulations, we expect up to $\simeq 50\%$ of the burned mass, or $\simeq 0.5 M_{\odot}$, to be ^{56}Ni. This is nearly enough to power a SNIa light curve.

There are several features of the computed explosion, however, that lead us to conclude that it is an incomplete model of a SNIa. One distinct feature is the presence of a massive, $\simeq 0.4 M_{\odot}$, outer layer of unburned CO surrounding burned matter. The presence of such a layer was a typical feature of all one-dimensional deflagration models with constant S_t or with S_t decreasing at the end of the explosion (Woosley & Weaver, Khokhlov 1991). The exception is the W7 deflagration model (Nomoto et al., 1976) which created intermediate mass elements at velocities up to $\simeq 14,000$km/s by maintaining a high deflagration speed and simultaneously avoiding rapid expansion of the outer layers. The simulations presented here show the decrease of the burning rate in the outer layers and are not consistent with the W7-like behavior. The presence of the unburned outer layer significantly limits the maximum expansion velocities of the intermediate mass elements, and this presents a difficulty for the spectra of SNIa at maximum and before maximum light. The observations and spectral analyses indicate that the line-forming region for the intermediate mass elements extends up to $\simeq 15,000$ and in some cases up to $\simeq 30,000$km/s in velocity space (Branch, 1981; Benetti et al. ,1991; Wells et al., 1994; Höflich, 1995; Höflich & Khokhlov, 1996; Lentz et al. 2000).

The simulations also show that the formation of intermediate mass elements in a three-dimensional deflagration explosion occurs throughout almost the entire WD, and that some intermediate mass elements may form very close to the WD center. This presents another difficulty for spectral modeling. The spectra of normal bright SNIa show that the minimum velocity of the line-forming region of Si is $\simeq 8,000-11,000$km/s (Höflich & Khokhlov, 1996), Ca, $\simeq 4,000-6,000$km/s (Fisher et al., 1997), Mg, $\simeq 13,000-14,000$km/s (Meikle et al., 1996; Höflich, 1997; Wheeler et al., 1998; Gerardy et al., 2000). There is also an indication that the minimum velocity of carbon in SN1990N (CII at 6580 A) is larger than 26,000 km/s (Fisher et al. 1997), which means that practically all of the material in this supernova has been burned. According to the simulations, unburned CO is also likely to remain in the central regions of the deflagration supernova where it will coexist with ^{56}Ni. Whether this can lead to the excitation of oxygen lines in the late-time spectra when the positron energy deposition becomes nonlocal (Milne et al. 1999)is an open question which requires further investigation (Höflich, private communication).

The formation of a massive outer layer of unburned material is a large-scale effect caused by the competition between the of buoyancy of large-scales structures (rising plumes) and the global expansion of the WD. In this competition, buoyancy eventually loses. During the explosion, the expansion velocity of the star increases gradually, and at 1.8, outer layers have velocities comparable or even exceeding the velocity of the large-scale plumes of burned products. Even if burning on small scales is underestimated in the simulation, increasing the energy released by small scales would increase the expansion velocity, but would hardly affect the buoyancy of the plumes. As the WD continues to expand into the vacuum, the rarefaction will accelerate the outer layers and this will further increase their velocity relative to the burned material.

The difficulties associated with the deflagration explosion can be avoided if burning turns into a detonation during the explosion (delayed detonation). Detonation would easily overcome the expansion and would incinerate the outer unburned layers of CO. This was one of the initial reasons for the introduction of the delayed detonation model of SNIa. It is also clear that the delayed detonation will help with the potential problems associated with three-dimensional effects by wiping out composition inhomogeneities in the inner layers.

These are the first simulations with the model presented in the paper. As such, they show new effects but also rais many questions. Computations with more resolution and with different subgrid burning models are required to determine if the resolved scales are small enough that

burning on these scales is in a self-similar regime. In particular, at maximum burning ($\simeq$ 1.5s), the simulations show large-scale motions with relative velocities of $\simeq 5 \times 10^8$cm/s. Thus there should be shear instabilities and a strong turbulent cascade on the sides of rising plumes. This should be incorporated into the model. The question of the deflagration-to-detonation transition (DDT) must also be addressed. A rough estimate can be made as follows. Assume that at 1.5s, the turbulent velocity is $\simeq 10^8$cm/s on the driving scale $L \simeq 10^8$cm. Then, from Kolmogorov cascade, the turbulent velocity $U_\lambda \simeq 10^5 \lambda$ cm/s on a scale λ, where λ is in centimeters. At $\rho \simeq 10^7$g/cc, the thickness of the laminar flame is $\delta_l \simeq 10^2$cm, and on the scale $\lambda \simeq \delta_l$ the velocity $U_\lambda \simeq 10^7$cm is much greater than S_l. Thus, the turbulent velocity on this scale may be strong enough to move the flame from the flamelet into the distributed regime, create hot spots of nonuniformly preheated unburned material, and thus trigger a detonation (Khokhlov et al., 1997). To trigger a detonation, the size of a nonuniform region must exceed a critical value which depends on density. At $\rho \simeq 10^7$g/cc, the critical size $\simeq 10^6$cm is much less than R_{WD} and the size of large scale structures obtained in the simulations. Thus the transition to detonation seems to be possible. Significant work requires to test these ideas. This paper shows that high-resolution three-dimensional modeling of SNIa is now a reality.

The calculations presented here indicate that the result of the explosion may be sensitive to varying the position of the ignition site and the initial carbon fraction X_C in a WD. Decreasing of X_C leads to less energy release and less buoyant products of burning. This results in much slower development of the RT-instability, so that the freezing due to expansion may be more effective. On the other hand, smaller energy release leads to slower expansion as well. It is most likely that decreasing X_C would result in a weaker explosion. Sensitivity to the position of the ignition site indicates that the results may also be sensitive to stellar rotation, which may lead to a preferential growth or suppression of the initial perturbations along the rotational axis. This makes both X_C and rotation potentially good candidates for being the 'hidden parameters' to describe the observed diversity of SNIa (Phillips, 1993).

Acknowledgments. I am grateful to Rob Rosenberg (NRL) and Almadena Chtchelkanova (Berkeley Research Associates) who developed FTT-based tools for the surface rendering and visualization used in this work. This paper benefited greatly from discussions with Peter Höflich (UT Austin), Elaine Oran (NRL), Craig Wheeler (UT Austin), Vadim Gamezo (Berkeley Research Associates), and Stirling Colgate (LANL). Work was supported in part by the Naval Research Laboratory through the Office of Naval Research and by the NASA ATP program.

References

Arnett, W.D. & Livne, E. 1994. ApJ 427, 314.

Benetti S., Cappellaro E., Turatto M. 1991, AA 247 410

Branch, D. 1981. ApJ, 248, 1076.

Colella, P. & Glaz, H.M. 1985. J. Comput. Phys., 59, 264.

Colella, P. & Woodward, P.R. 1984. J. Comput. Phys., 54, 174.

Fisher A., Branch D., Höflich P., Khokhlov A. 1995. ApJ 447L, 73.

Fisher A., Branch D., Nugent P., Baron E. 1997, ApJ 481L, 89.

Fowler, W.A., Caughlan, G.R. & Zimmerman, B.A. 1975. ARA&A, 13, 69.

Gamezo, V.N., Khokhlov, A.M. & Oran, S.E., Proceedings of the 17th International Colloquium on the Dynamics of Explosions and Reactive Systems, Universität Heidelberg, IWR, 1999.

Gamezo, V.N., Vasil'ev, A.A., Khokhlov, A.M. & Oran, S.E., Proceedings of the 28th International Symposium on Combustion, vol.28, 2000 (in press).

Gerardy C., Höflich P., Fesen R., Wheeler J.C. 2000, AJ, to be submitted

Hillebrandt, W. & Niemeyer, J.C 2000. astro-ph/0006305

Höflich, P. 1995. ApJ 443, 89.

Höflich P. 1997, in: Second Oak Ridge Symposium on Atomic & Nuclear Astrophysics, ed. A. Mezzacappa, IOP Publishing, p. 693

Höflich & Khokhlov 1996, ApJ 457, 500

Khokhlov, A.M. 1991. A&A, 245, 114.

Khokhlov, A.M. 1995. ApJ, 449, 695.

Khokhlov, A.M., Oran, E.S., Wheeler, J.C. 1997. ApJ, 478, 678.

Khokhlov, A.M. 1998. J. Comput. Phys., 143, 519.

Khokhlov, A.M. & Chtchelkanova, A.Yu. 1999. Proceedings of the 9-th SIAM Conference on Parallel Processing for Scientific Computing, San Antonio, TX, March 22-24, 1999.

Khokhlov, A.M., Höflich, P.A., Oran, E.S., Wheeler, J.C., Wang, L. & Chtchelkanova, A.Yu. 1999. ApJ, 524, L107.

Khokhlov, A.M. & Oran, S.E. 1999. Combustion & Flame, 119, 400.

Langanke, K. & Martinez-Pinedo, G. 1999. Phys. Lett. B., 453, 187.

Lapidus, A. 1967. J. Comput. Phys. 2, 154.

Lentz, E.J., Baron, E., Branch, D., Hauschieldt, P.H. 2000. ApJ, submitted; astro-ph/0007320.

Livne, E. 1993. ApJ 415, L17.

Martinez-Pinedo, G., Langanke, K. & Dean, D.J. 2000. ApJ, 126:493.

Meikle W.P.S., Cumming, , R.J., Geballe, T.R., et al. 1996. MNRAS 281, 263.

Milne P. A., The, L.-S.; Leising, M. D. 1999, ApJS 124, 503

Nomoto, K., Sugimoto, D. & Neo, S. 1976. AP&SS, 39, L37.

Nomoto, K., Thielemann, F.-K., Yokoi, K. 1984. ApJ, 286, 644.

Perlmutter, S., Aldering, G., Goldhaber, G., et al. 1999. ApJ, 517:565.

Phillips, M.M. 1993. ApJ, 413, L105.

Pskovskii, I. p. 1977. Soviet Astronomy, 21, 675.

Reinecke, M., Hillebrandt, W. & Niemeyer, J.C. 2000. A&A, in press.

Riess, A.G., Filippenko, A.V., Lui, M.C., et al. 2000. ApJ, 563:62.

Timmes, F. & Woosley, S.E. 1992. ApJ, 396, 649.

Wells L.A., Phillips M.M., Suntzeff B. et al. 1994. AJ 108, 2233.

Wheeler J.C., Höflich P., Harkness R., Spyromillo J. 1998, ApJ 496, 908

Woosley, S.E. & Weaver, T. 1986. ARA&A, 24, 205.

Figure captions

Figure 1a. - Figure 1a. - Total (E_{tot}), kinetic (E_k), released nuclear (E_n) energy and burned mass M_b of a $\frac{1}{2}C + \frac{1}{2}O$ WD during a deflagration explosion (Section 3.2).

Figure 1b. - Solid line - kinetic energy (E_k) of a $\frac{1}{2}C + \frac{1}{2}O$ WD during a deflagration explosion at earlier times (Section 3.2). Dashed line - kinetic energy with burning turned off (Section 3.1).

Figure 2a. - Time evolution of the flame surface during a deflagration explosion (Section 3.2).

Figure 2b. - Same as Fig. 2a. Details of the flame structure at 1.8s.

Figure 3. - Flame variable f (Equation (2)) for a deflagration explosion Section 3.2 at 1.44s shown in three orthogonal planes offset by 3.2×10^7cm from the WD center.

Figure 4. - Same as Figure 3 but shows the radial velocity.

Figure 5. - Estimated turbulent flame speed S_t (Equation (15)) during a deflagration explosion Section 3.2.

Figure 6. - Flame variable f (Equation (2)) for a deflagration explosion Section 3.2 at the end of the simulation 1.8s shown in three orthogonal planes offset by 3.2×10^7cm from the WD center.

Figure 7. - Same as Figure 6 but shows the radial velocity.

Figure 8. - Mesh and flame variable f in the X-Y plane passing through the WD center for a deflagration explosion Section 3.2 at the end of the simulation $t = 1.8$s.

Figure 9a. - Density and velocity in the X-Z plane passing through the WD center for a deflagration explosion Section 3.2 at the end of the simulation 1.8s. The region $x = 1.2 \times 10^8$cm and $z = 0 - 9.4 \times 10^7$cm is shown.

Figure 9b. - Mesh in the X-Z plane passing through the WD center for a deflagration explosion Section 3.2 at the end of the simulation 1.8s. The region $x = 1.2 \times 10^8$cm and $z = 0 - 9.4 \times 10^7$cm is shown.

Figure 10. - Time evolution of the total (E_{tot}), kinetic (E_k), released nuclear (E_n) energy and burned mass M_b of a $\frac{1}{2}C + \frac{1}{2}O$ WD during a deflagration explosion with the laminar flame speed $S = S_l$ (Section 3.3).

Figure 11. - Flame surface in the X-Y plane at $\simeq 1.3$s for the simulation with (right panel, Section 3.2) and without (left panel, Section 3.3) turbulent small-scale burning.

Figure 12. - Distribution of the Fe-group, Si-group, and CO matter for a deflagration explosion Section 3.2 at the end of the simulation $t = 1.8$s shown in three orthogonal planes offset by 3.2×10^7cm from the WD center.

Figure 13. - Same as Figure 12 but shows the neutron excess $\eta = 1 - 2Y_e$.

Figure 14. - Deflagration starting with the offset ignition point (Section 3.5). Shows the flame variable and velocity at $\simeq 1$s. Black square shows the ignition point.

Figure 15. - Evolution of the kinetic energy during deflagration explosion of a WD with the initial $0.5C + 0.5O$ and $0.2C + 0.8O$ compositions (Section 3.5).

This figure "fig1a.png" is available in "png" format from:

http://arxiv.org/ps/astro-ph/0008463v1

This figure "fig1b.png" is available in "png" format from:

http://arxiv.org/ps/astro-ph/0008463v1

This figure "fig2a.jpg" is available in "jpg" format from:

http://arxiv.org/ps/astro-ph/0008463v1

This figure "fig2b.jpg" is available in "jpg" format from:

http://arxiv.org/ps/astro-ph/0008463v1

This figure "fig3.jpg" is available in "jpg" format from:

http://arxiv.org/ps/astro-ph/0008463v1

This figure "fig4.png" is available in "png" format from:

http://arxiv.org/ps/astro-ph/0008463v1

This figure "fig5.png" is available in "png" format from:

http://arxiv.org/ps/astro-ph/0008463v1

This figure "fig6.jpg" is available in "jpg" format from:

http://arxiv.org/ps/astro-ph/0008463v1

This figure "fig7.jpg" is available in "jpg" format from:

http://arxiv.org/ps/astro-ph/0008463v1

This figure "fig8.png" is available in "png" format from:

http://arxiv.org/ps/astro-ph/0008463v1

This figure "fig9.jpg" is available in "jpg" format from:

http://arxiv.org/ps/astro-ph/0008463v1

This figure "fig10.png" is available in "png" format from:

http://arxiv.org/ps/astro-ph/0008463v1

This figure "fig11.jpg" is available in "jpg" format from:

http://arxiv.org/ps/astro-ph/0008463v1

This figure "fig12.png" is available in "png" format from:

http://arxiv.org/ps/astro-ph/0008463v1

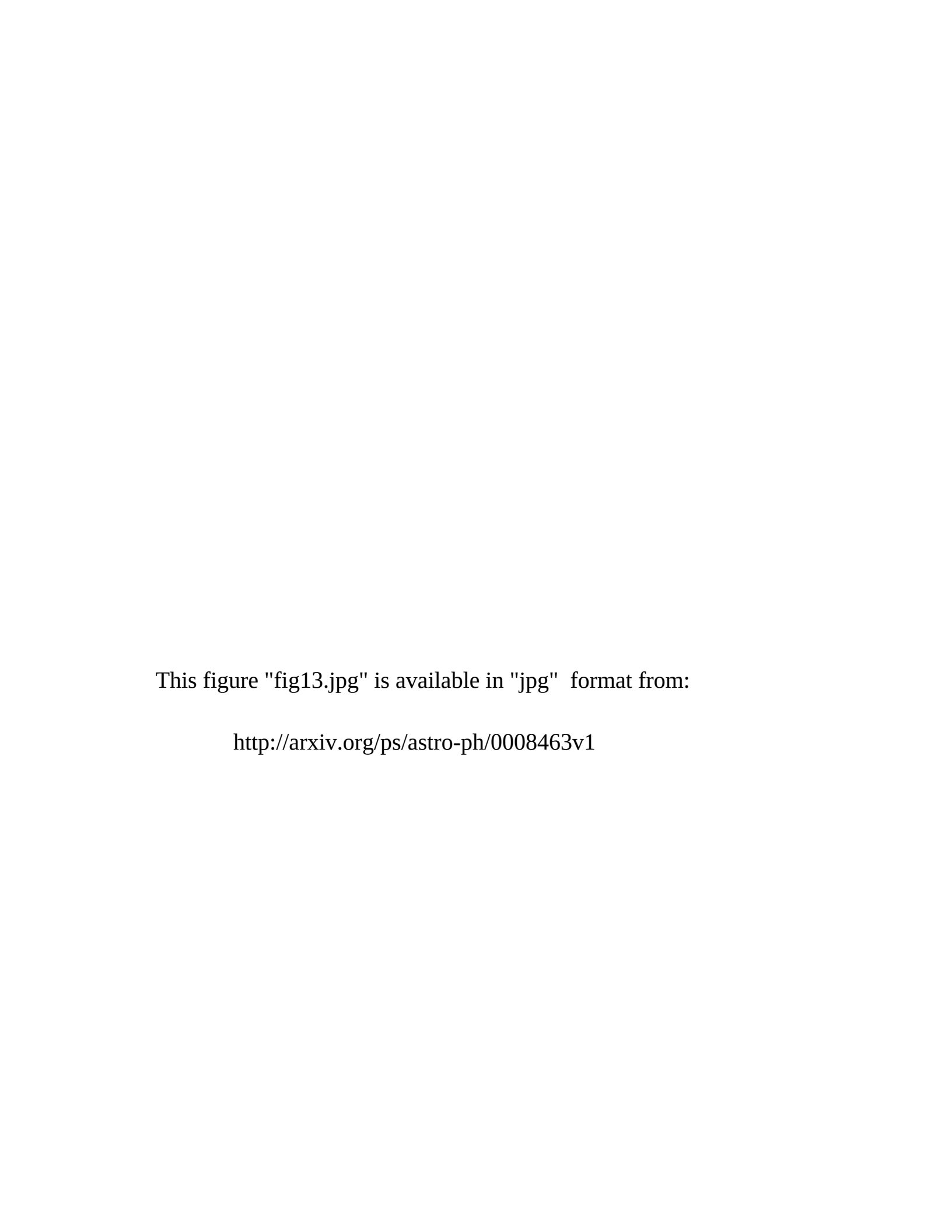
This figure "fig13.jpg" is available in "jpg" format from:
http://arxiv.org/ps/astro-ph/0008463v1

This figure "fig14.png" is available in "png" format from:

http://arxiv.org/ps/astro-ph/0008463v1

This figure "fig15.png" is available in "png" format from:

http://arxiv.org/ps/astro-ph/0008463v1